



## Radio Science

### RESEARCH ARTICLE

10.1002/2013RS005272

#### Key Points:

- Structure classification of high-resolution ESF data
- Power law characteristics vary
- Two-component power law confined to low-altitude high-density regions

#### Correspondence to:

C. L. Rino,  
crino@comcast.net

#### Citation:

Rino, C. L., C. S. Carrano, and P. Roddy (2014), Wavelet-based analysis and power law classification of C/NOFS high-resolution electron density data *Radio Science*, 49, 680–688, doi:10.1002/2013RS005272.

Received 27 JUL 2013

Accepted 7 AUG 2014

Accepted article online 12 AUG 2014

Published online 25 AUG 2014

## Wavelet-based analysis and power law classification of C/NOFS high-resolution electron density data

C. L. Rino<sup>1</sup>, C. S. Carrano<sup>1</sup>, and Patrick Roddy<sup>2</sup>

<sup>1</sup>Institute for Scientific Research, Boston College, Chestnut Hill, Massachusetts, USA, <sup>2</sup>Institute for Scientific Research, Air Force Research Laboratory, Albuquerque, New Mexico, USA

**Abstract** This paper applies new wavelet-based analysis procedures to low Earth-orbiting satellite measurements of equatorial ionospheric structure. The analysis was applied to high-resolution data from 285 Communications/Navigation Outage Forecasting System (C/NOFS) satellite orbits sampling the postsunset period at geomagnetic equatorial latitudes. The data were acquired during a period of progressively intensifying equatorial structure. The sampled altitude range varied from 400 to 800 km. The varying scan velocity remained within 20° of the cross-field direction. Time-to-space interpolation generated uniform samples at approximately 8 m. A maximum segmentation length that supports stochastic structure characterization was identified. A two-component inverse power law model was fit to scale spectra derived from each segment together with a goodness-of-fit measure. Inverse power law parameters derived from the scale spectra were used to classify the scale spectra by type. The largest category was characterized by a single inverse power law with a mean spectral index somewhat larger than 2. No systematic departure from the inverse power law was observed to scales greater than 100 km. A small subset of the most highly disturbed passes at the lowest sampled altitudes could be categorized by two-component power law spectra with a range of break scales from less than 100 m to several kilometers. The results are discussed within the context of other analyses of in situ data and spectral characteristics used for scintillation analyses.

### 1. Introduction

Physics-based models of equatorial spread  $F$  (ESF) characterize the evolution of large-scale structure [Retterer, 2010]. The review by Hysell [2000] contains an overview of physics-based models with supporting in situ observations. Briefly, the postsunset  $F$  region is lifted upward by atmospheric dynamo electric fields. Perturbations on the unstable bottom side of the  $F$  layer initiate electron density depletions that can extend upward more than 1000 km. The active region comprises flux tubes within east-west spans of thousands of kilometers. At a fixed ground-observing station frequency-dependent activity can be detected from dusk until well after midnight. Plume-like images from consecutive HF radar range-angle-intensity records delineate the active regions. Structure models used to interpret measurements and predict structure beyond the measurement space must contend with a large inhomogeneous and anisotropic ionospheric region with embedded structure subtending intermediate scales from hundreds of kilometers to tens of meters.

ESF observations include in situ probes, which measure one-dimensional scans of observable parameters; VHF radars, which measure Bragg wavelength (meter-scale) electron density structure within the radar beam; and radio frequency scintillation, which measures the cumulative effects of electron density structure intercepted along the propagation path. Statistical structure models are essential for in situ and remote sensing data interpretation. Robust statistical measurement requires selection of processing intervals and model parameter extraction. A wavelet-based analysis procedure was developed to formalize and automate segmentation and classification operations. This paper applies the analysis procedures to a large body of intermediate-scale high-resolution in situ data obtained from the Communications/Navigation Outage Forecasting System (C/NOFS) satellite.

Intermediate-scale structure subtends the scale range from hundreds of kilometers to hundreds of meters. High-resolution ion density data from the C/NOFS planar Langmuir probe (PLP) instrument are well suited for intermediate-scale structure analysis. A description of the instrument and its capabilities can be found in Rodrigues *et al.* [2009]. Figure 1 shows a standard display of C/NOFS ion density data. The blue sinusoidal

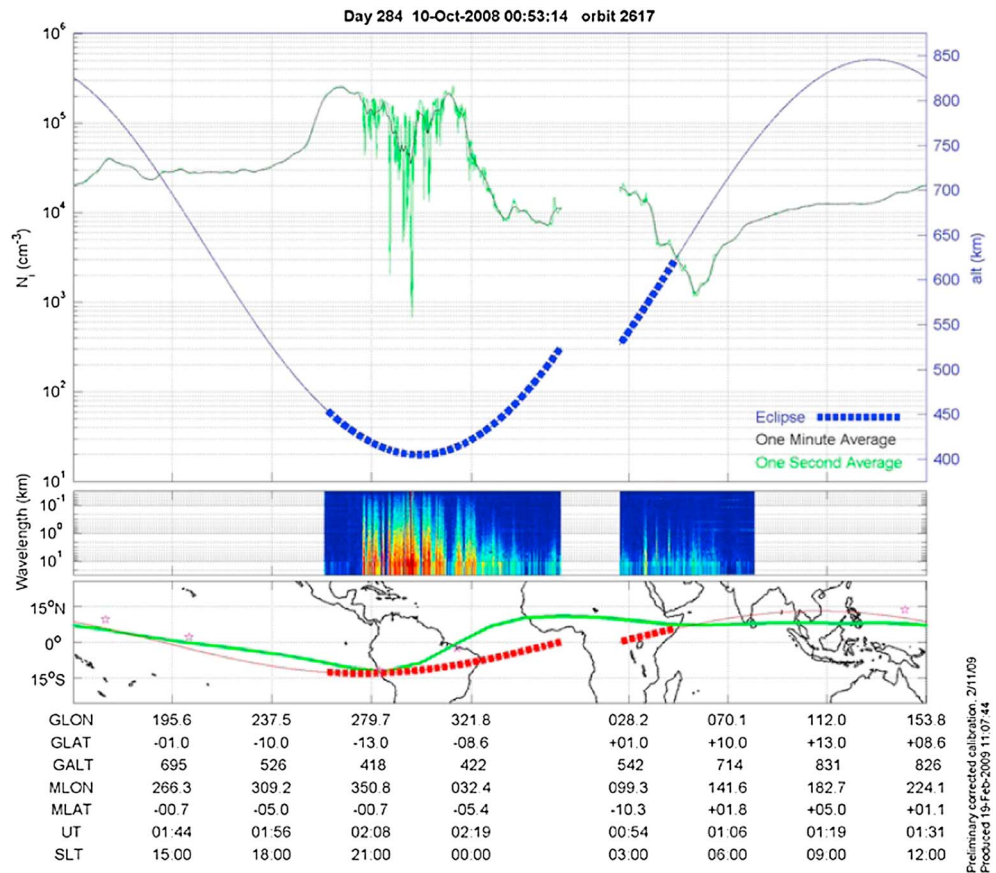


Figure 1. Summary display of data from Langmuir probe carried by the C/NOFS satellite.

curve shows altitude on the right-hand scale with the period of eclipse indicated by filled squares. The black curve in the upper frame is a 1 min average of the low-resolution PLP reports.

High-resolution data extracted from a local nighttime segment at 512 Hz but averaged for display are superimposed in green. A maximum entropy spectrogram superimposed below the upper frame highlights

varying spatial wave number distributions obtained from 10 km intervals. Self-explanatory geographic, geomagnetic, and time data are listed below the map overlay. Consecutive orbits sample the structure evolution at approximately 100 min intervals.

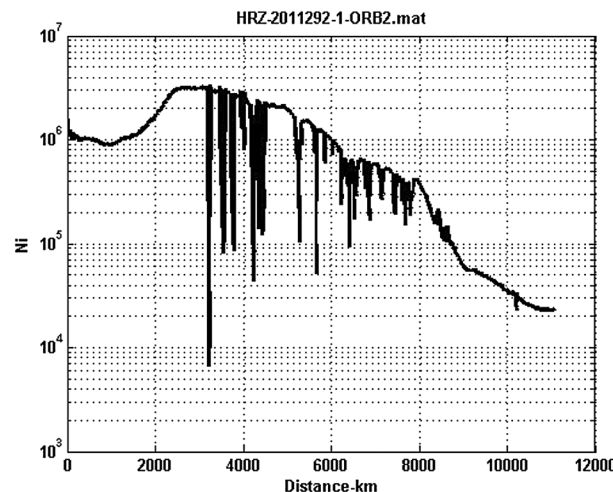
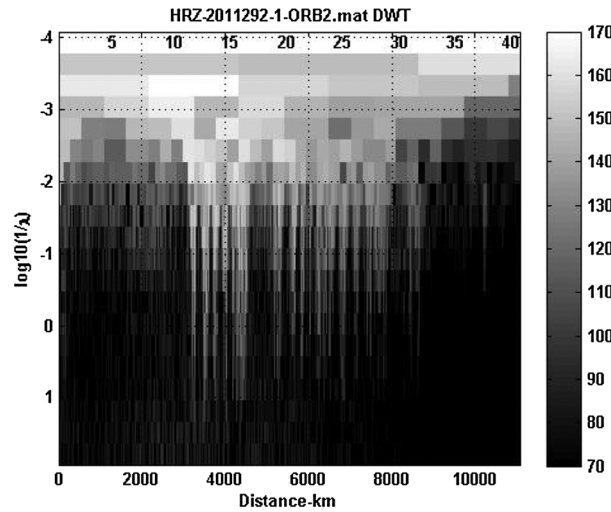


Figure 2. High-resolution data from 2011 day 292 orbit 2. The distance scale is the length of the C/NOFS scan.

The first step in the analysis procedure computes a discrete wavelet transform (DWT) over the entire data set. When applied to a data set with  $2^d$  samples, DWTs generate  $d$ -resolved scales. The wavelet that generates the resolved scale with index  $j$  is nonzero over an interval of length  $2^{(j-d)}Y$ , where  $Y$  is the data length. Thus, the spatial resolution and the number of independent DWT samples at each scale increase as the scale decreases. The largest segment that supports averaging



**Figure 3.** Gray scale decibel display of the DWT computed from the data shown in Figure 2. The numbers at the top of the display are the center points of the indicated segments.

can be identified by observing the DWT variation at each scale. As will be described in more detail below, a wavelet-scale spectrum is computed for each segment.

Segment classification is based on a hypothesized two-component spectral density function (SDF) of the form

$$\varphi(q) = \begin{cases} c_s^1 q^{-p_1} & q_{\min} \leq q < q_0 \\ c_s^2 q^{-p_2} & q_0 \leq q < q_{\max} \end{cases}, \quad (1)$$

where  $q = 2\pi/s$  represents the magnitude of spatial wave number associated with the spatial scale with support  $s$ . The relation between the one-dimensional scale being measured and the anisotropic structure being sampled generally involves representing  $q$  as the square root of a generalized quadratic form. For data analysis only the magnitude of  $q$  needs be consid-

ered. Imposing SDF continuity at the break wave number  $q_0$  introduces a dependency that constrains the parameter space, whereby only three of the four defining parameters are independent. The classification procedure estimates the turbulent strength parameters  $c_s^1, c_s^2$ ; the power law index parameters  $p_2, p_1$ ; the power law scale ranges; and the overall log linear least squares error. For a good model fit,  $c_s \sim c_s^1$  and  $c_s q_0^{(p_2-p_1)} \sim c_s^2$ . For these SDFs the break wave number can be estimated from the continuity relation

$$q_0 = \exp \left\{ \left( \ln c_s^2 - \ln c_s^1 \right) / \left( p_2 - p_1 \right) \right\}. \quad (2)$$

The model encompasses a broad range of structure types. If  $p_1 \sim p_2$ , the SDF is classified as a single power law. If  $p_1 \sim 0$ , the break parameter  $q_0$  is effectively a measure of the outer scale. If  $p_2 \sim 0$ , the SDF is noise limited. Finally, if  $p_2 > p_1$  the SDF is classified as two component. The homogeneous power law scale range is determined by  $q_{\min}$ , which is constrained by the segmentation, and  $q_{\max}$ , which is determined by the spatial resolution.

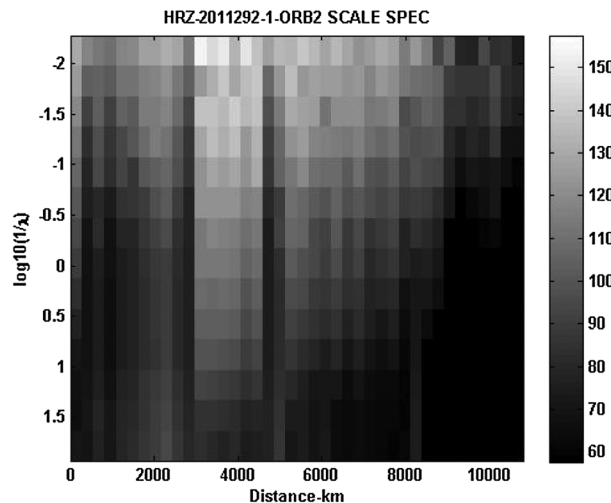


**Figure 4.** Scalogram derived from the DWT shown in Figure 3.

## 2. C/NOFS Data Analysis

C/NOFS PLP data are reported in 1 s frames with supporting data provided for each frame. High-resolution frame sampling is confined to the most likely ESF periods. To apply the wavelet-based analysis procedure, high-resolution data sampled at 512 Hz from each orbit must be identified, extracted, and edited to remove periodic instrument calibration breaks. The data must also be translated from uniform time to uniform spatial sampling.

The 512 Hz high-resolution records are extracted and edited. Satellite positions for each frame are reported in GPS coordinates. The GPS reports are converted to a topocentric coordinate

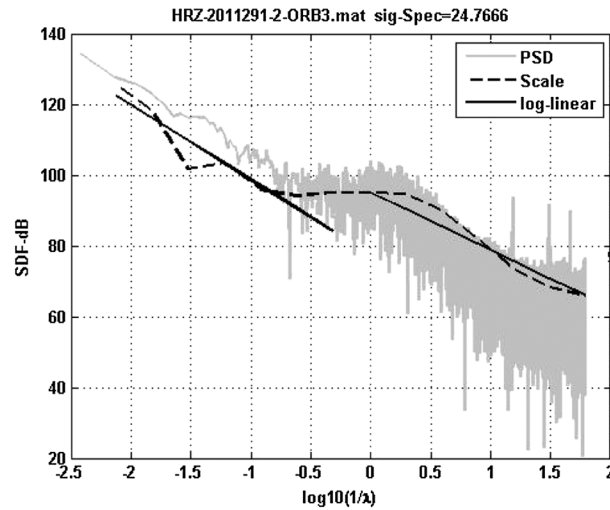


**Figure 5.** Example of poor model fit. The offset scale spectrum is shown dashed, with log linear fits solid. The periodogram is overlaid in grey for reference.

The preprocessed data record contains 1,033,464 density samples interpolated here to 8.24 m intervals as described above. A folded periodic extension to  $N_{\text{ext}} = 2^{21} = 2,097,152$  samples is used for efficient DWT computation. The 21 DWT scales are converted to reciprocal spatial wavelengths by the equivalence

$$q_j / (2\pi) = 2^{(j-1)} / (2\Delta s) \text{ for } j = 1, 2, \dots, J_{\text{max}}, \quad (3)$$

where  $J = \log_2(N_{\text{ext}})$ ,  $J_{\text{max}}$  is the index that defines the segmentation, and  $\Delta s$  is the sample interval. As already noted, each scale indexed by  $j$  supports  $2^{J-j}$  DWT samples. Computation of the DWT requires no prior operations other than data extension to the nearest larger power of 2. Moreover, the DWT can be inverted to recover the original data without error or to explore scale-dependent reconstruction.

Figure 3 is a gray scale display of the DWT intensity in decibel units. The ordinate is  $\log_{10}(q_j / (2\pi))$  with  $\Delta s$  measured in kilometers. Thus, 0 corresponds to 1 km. Negative values correspond to larger scales. Positive values correspond to smaller values. For display purposes, the independent measures at each wave number

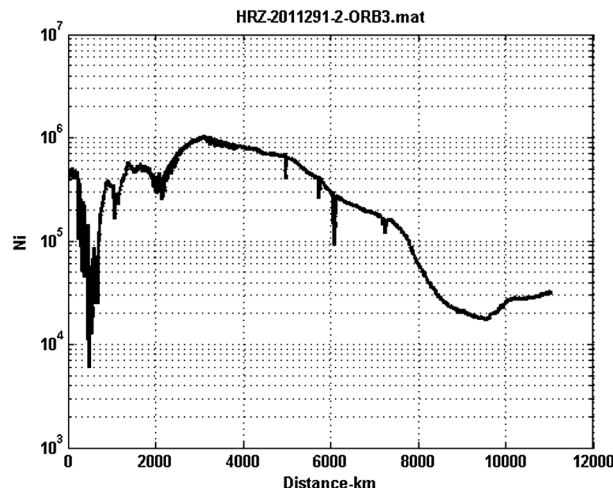


**Figure 6.** High-resolution data extracted from day 291 orbit 3. The spectral summary shown in Figure 5 is from segment 9.

system (tcs) tangent to the reference ellipsoid at the start of the pass. The tcs reports are interpolated to generate a three-dimensional position for each sample. The three-dimensional positions are used to generate sample-to-sample path distances. A histogram of the path differences identifies the most probable sample interval. The data set is interpolated to generate uniform spatial samples at the most probable spatial interval. The variation of the unrectified sample intervals is typically less than 5 m. Figure 2 shows a rectified high-resolution data set. The data set spans more than 10,000 km. The density varies over 2 orders of magnitude.

## 2.1. Wavelet-Based Analysis

### 2.1.1. Discrete Wavelet Transforms and Scale Spectra

The example summarized in Figure 2 will be used to illustrate the analysis procedure.

have been repeated to fill out  $N_{\text{ext}}$  samples at each scale. The DWT has been truncated at the limits of the original data interval. The wavelets that straddle the data extension are influenced by the folded periodic extension, but only the edge wavelet sample is affected.

One can see by inspection of the DWT display that the largest scales contain too few independent samples for reliable statistical averaging. However, wavelet scales below a specified level  $J_{\text{max}} \leq J$  support at least  $2^{J-J_{\text{max}}}$  samples. A segmentation is defined by accepting scales to  $J_{\text{max}} < J$ . Because of the uniformity of the C/NOFS orbits, a single segmentation with  $2^{15} = 32,768$  samples per segment could be used for all the high-resolution data sets. With the segmentation defined, scale spectra from

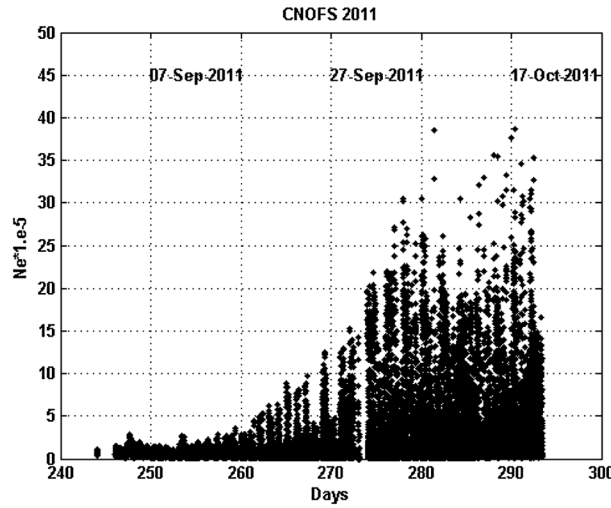


**Figure 7.** Segment maximum electron density versus fractional UT day number.

each segment can be computed by averaging the independent DWT estimates within each segment. The extended data span supports 64 segments, 40 of which coincide with the original data.

Scale spectra are particularly well suited for estimation of inverse power law structure. However, there is a wavelet-dependent bias in the turbulent strength parameters derived from scale spectra. Although the bias can be computed from the wavelet definition, it is convenient to use the unwindowed SDF.

$$SDF_n = \left| \sum_{k=0}^{N-1} N_k \exp \{ 2\pi i n k / N \} \right|^2 \quad (4)$$

Because  $N_k$  is real, only the positive spatial wave numbers

$$k_n / (2\pi) = -n / (N\Delta s) \text{ for } 1 \leq n \leq N/2 + 1, \quad (5)$$

need be considered. With  $N$  equal to the number of samples in the segment,  $k_n/\pi$  spans the same range as the wavelet scales  $q_j/(2\pi)$ . A polynomial fit to the SDF is used to generate a common sampling for computation of  $10 \log_{10}(SDF_j)$ . Adding the offset

$$O = \frac{1}{J_{\max}} \sum_{j=1}^{J_{\max}} \left( \overline{10 \log_{10}(SDF_j)} - 10 \log_{10}(S_j) \right), \quad (6)$$

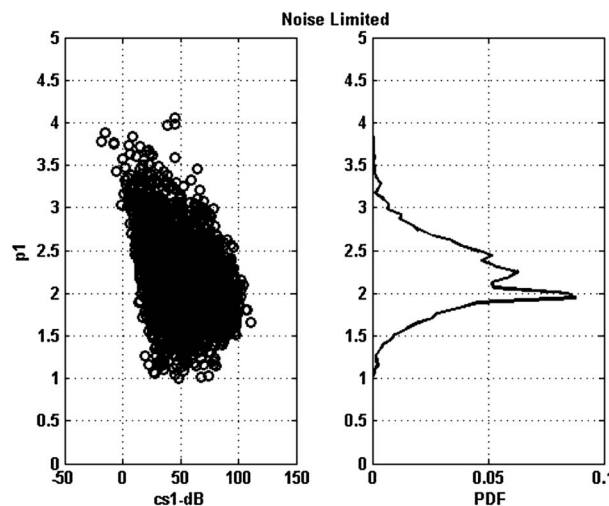
to the decibel scale spectra aligns the scale spectrum with the corresponding SDF.

Figure 4 shows the scalogram derived from the segmentation. The scalogram is a smoothed version of the DWT shown in Figure 3 offset to match the SDF intensity range. The scalogram and the spectrogram formally support the same dynamic range. However, the corresponding spectrogram (not shown) does not reveal average spectral details as clearly because it has no intrinsic spatial-frequency smoothing. Standard Discrete Fourier Transform processing uses similar averaging, but the windowing necessary to manage edge

discontinuities distorts the low-frequency content. The maximum entropy method (MEM) [Fougere, 1985], which is used extensively for ESF spectral estimation, imposes an autoregressive data model to extract a smoothed spectral estimate. Although the autoregressive model supports multiple power law SDFs, it has no intrinsic connection to power law processes, and it provides no guidelines for segmentation. With fast DWT algorithms, MEM and wavelet-based analyses have similar computational requirements.

### 2.1.2. Parameter Extraction and Classification Summary

The offset scale spectrum from each segment is a logarithmically spaced set of  $J_{\max}$  samples, denoted  $dB S_j$ . A log linear least squares fitting procedure generates



**Figure 8.** Summary of 17,159 noise-limited and single power law segments.

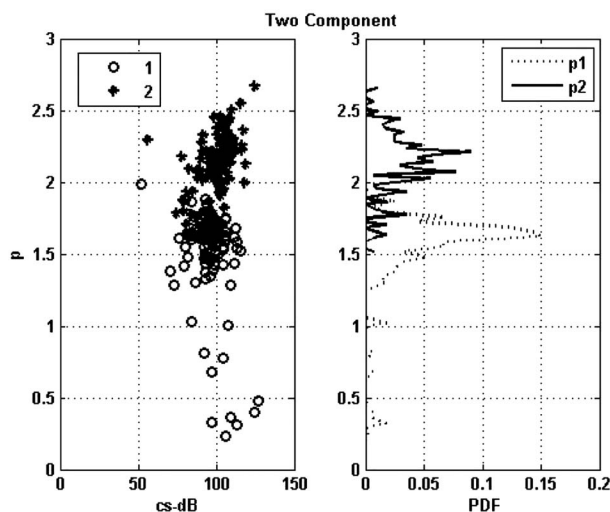


**Figure 9.** Summary of 401 two-component power law segments.

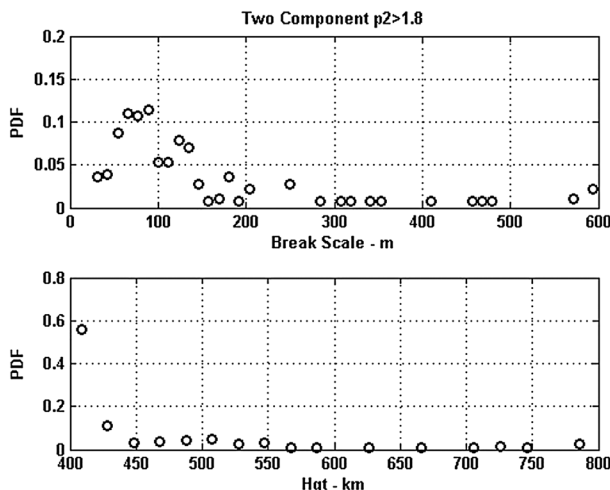
two-component power law fit parameters  $c_s^1$ ,  $p_1$ ,  $c_s^2$ , and  $p_2$ ; power law scale ranges; and the overall log linear least squares error. Aside from the offset to remove the wavelet intensity bias, the classification uses only the scale spectra.

The first level of classification excludes segments with structure poorly fit to the power law model. An example of an excluded segment is shown in Figure 5, which is segment 9 from the high-resolution orbit summarized in Figure 6. Segment 9 is from the decay phase of more fully developed structure observed in earlier orbits. The structure is concentrated in a plateau from 6 km to 0.5 km.

A significant difference between the wavelet-based analysis and other published analyses is the large 262 km segment length, which was derived from the DWT shown in Figure 3 as described. Simulations were used to verify that scale spectra correctly extract power law parameters to scales approaching the segmentation. However, the estimates are stochastic and vary accordingly.

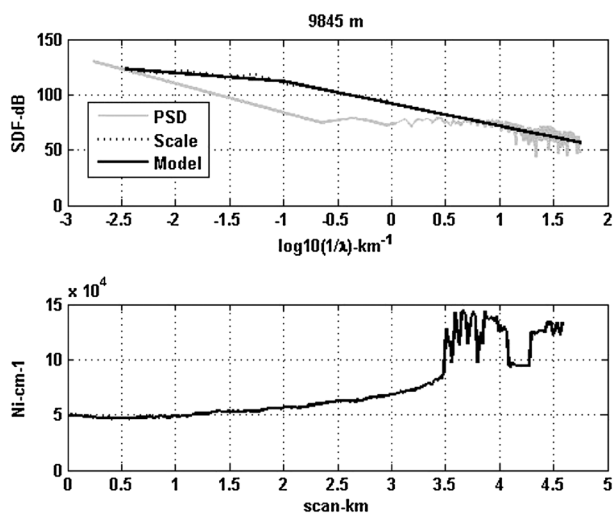
The wavelet-based classification and parameter extraction was applied to 79,664 segments of which 18,102 (23%) supported structure that could be classified using the generalized power law model (1). The small fraction of segments that admit statistical classification is attributed to the high degree of spatial variability in structure evolution. Spectra with  $p_1 \sim p_2$  and  $c_s^1 \sim c_s^2$  are classified as single component. Spectra with  $p_1 < p_2$  and a well-developed break scale derived from (2) are classified as two component. However, the C/NOFS instrument characteristics limit high-resolution measurements to structures with sufficiently high electron density. Thus, the smallest measurable spectral wave number is limited by either resolution or uncorrelated samples with a high wave number tail characterized by  $p_2 \sim 0$ . Although the limitation is not additive noise, an intermediate noise-limited category was introduced to capture these segments.

Figure 7 is a display of the maximum electron density achieved in each contributing segment versus day number. The plot shows that the C/NOFS data were acquired during a period of progressively increasing electron density. Enhanced ESF activity is expected under these conditions, which often follow a coronal mass ejection.



**Figure 10.** (top) A histogram of the tail segment break scales. (bottom) A histogram of the tail segment heights.

The single power law classification was the largest population. However, because noise-limited spectra sample common structure up to the smallest resolved scale, the  $p_1$  and  $c_s^1$  parameters for the noise-limited spectra were included in the single power law category. The left-hand frame of Figure 8 is a scatter diagram of the combined  $p_1$  and  $c_s^1$  parameters. The right-hand frame is a histogram of the  $p_1$  values. There is a peak in the distribution at  $p_1 = 2$ , which is the signature of an edge-dominated structure. An investigation of the spectra with  $p_1 = 2$  showed that they contained a near-discontinuous change, which can

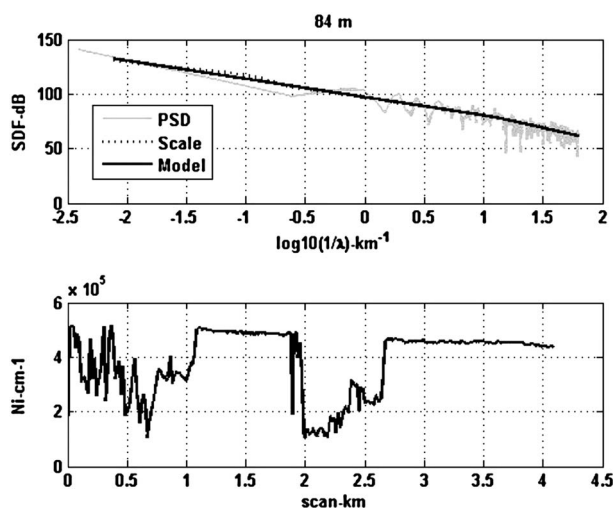


**Figure 11.** Example of scale spectrum and two-component power law model evaluated with extracted parameters. Large break scale is listed.

be attributed to a near orthogonal intercept of a plume wall. The dominant single power law  $p1$  distribution is broad distribution with a most probable value steeper than 2. There is also an inverse correlation between  $p1$  and  $c_s^1$ . This pattern was observed in data from rocket probes of ESF structure [Rino et al., 1981].

Although the remaining segments could all be classified as two component, the segments that fit the two-component category were restricted to segments that provided a good enough fit to (2) to generate a break scale estimate. Figure 9 summarizes the 401 segments that were so classified. The component 1 parameters are shown solid. The component 2 parameters are shown dashed. The component 1 spectral index distribution has a peak near  $p1 = 1.7$  with an extended tail of shallower values corresponding to the most highly disturbed passes. Figure 10 shows histograms of the measured break scales (top) and the segment heights. The broad range of break scales was unexpected, as will be discussed in the next section.

To probe the analysis method further, fits with large, small, and intermediate break scales are explored further here. Figure 11 (top) shows the model SDF (solid), the scale spectrum (dashed), and the unwindowed SDF (grey). Figure 11 (bottom) shows the data segment, which was structured only over a portion of the 260 km segment. The large disparity between the conventional SDF and the scale spectrum undoubtedly compromises the calibration, but in spite of the inhomogeneity the wavelet-scale spectra identifies a scale distribution. Figure 12 shows the same summary for an SDF closer to other published results, which are discussed in the following section. The configuration does have a broad distribution over two regions. Figure 13 shows a mix of large and smaller scales. However, none of the current results showed a kilometer scale break transitioning to a power law index approaching 3.



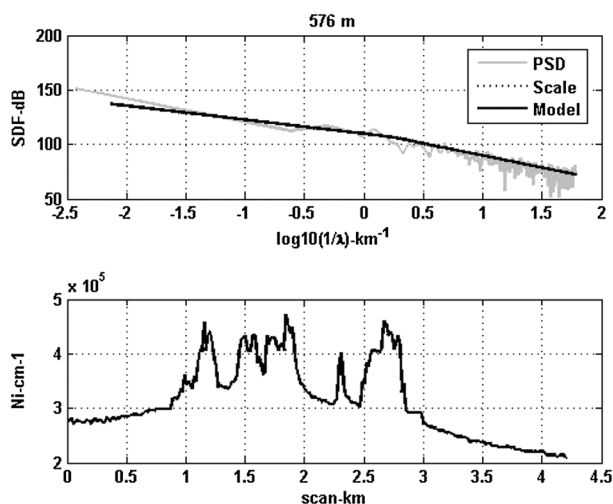
**Figure 12.** Example of scale spectrum and two-component power law model evaluated with extracted parameters. Small break scale is listed.

Figure 12 shows the same summary for an SDF closer to other published results, which are discussed in the following section. The configuration does have a broad distribution over two regions. Figure 13 shows a mix of large and smaller scales. However, none of the current results showed a kilometer scale break transitioning to a power law index approaching 3.

Figure 13 shows a mix of large and smaller scales. However, none of the current results showed a kilometer scale break transitioning to a power law index approaching 3.

### 3. Discussion

The first systematic study of in situ data that reported two-component spectra by Basu et al. [1983] used in situ data from the Atmosphere Explorer E satellite retarding potential analyzer. Four equatorial passes were analyzed using MEM spectral analysis over 10 km segments. A 25-sample subset comprising the most highly disturbed data segments showed two-component spectra with a most probable break at a wave number scale corresponding to approximately 500 m. The large- and small-scale indices were reported as 1 to 1.5 and 3 to 3.5, respectively. Their analysis of coincident scintillation data associated the enhanced structure with propagation disturbances on coincident paths.



**Figure 13.** Example of scale spectrum and two-component power law model evaluated with extracted parameters. Intermediate break scale is listed.

The discovery of the two-component intermediate-scale power law spectra resolved a long-standing dilemma regarding the frequency dependence of ESF scintillation. Simultaneous measurements of ESF disturbances at VHF, UHF, and gigahertz frequencies could not be reconciled with a single-component power law structure distribution. With a one-dimensional index greater than 2, which corresponds to a path-integrated phase spectral index of 3, strong-scatter theory predicts a scintillation index maxima greater than one with increasing Fresnel radius increases. Beyond the peak, the scintillation index decreases to a constant value near unity. As a consequence, the scintillation index in the gigahertz range can exceed the scintillation index at both VHF and UHF.

Simulations performed by Franke and Liu [1983] showed that the two-component structure reported by Basu et al. [1983] mitigates the strong focusing just enough to reconcile measured scintillation over the typical radio frequency range. Analyses of data from rocket probes of bottom-side ESF structure showed similar two-component power law spectra [Rino et al., 1981; Livingston et al., 1981; Kelley et al., 1982].

Theoretical support for a two-component power law structure comes from constrained two-dimensional turbulence [Ouelette, 2012]. In the ionosphere the development of turbulent structure is constrained to the cross-field direction. A feature of constrained two-dimensional turbulence is a two-component power law with an upward cascade in the large-scale region and a downward cascade in the small-scale region. Alternatively, it may be a characteristic of the exchange instability as discussed by Hysell and Kelley [1997].

Recent studies by Costa et al. [2011] address the objectives of the C/NOFS program directly. C/NOFS was launched to exploit physics-based models, propagation theory, and real-time measurements for propagation outage forecasting. To model the structure Costa et al. [2011] used a product spectral model with highly correlated Gaussian structure along the field lines and a power law distribution across field lines. The fitting procedure employed by Costa et al. [2011] is quite involved, but direct comparisons can be made to

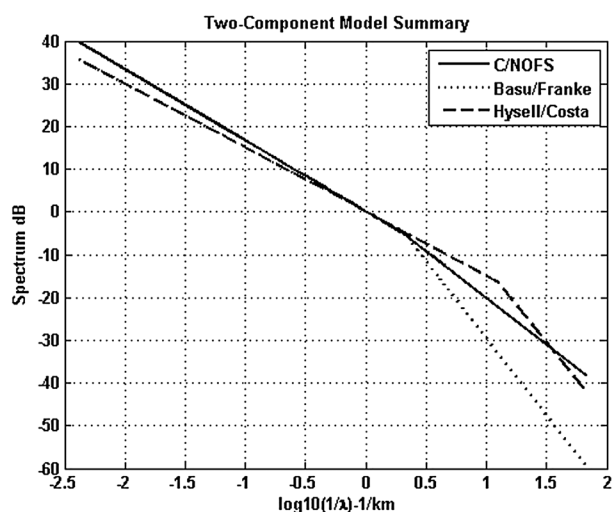


**Figure 14.** Two-component model with median parameters from two-component segments.

the one-dimensional spectra and model parameters shown in their Figure 4, which summarizes 12 MEM spectra used in the reported study. These results place the break scale at 80 m, which is consistent with the rocket results summarized by Hysell [2000]. Similar results have been reported more recently by Nishioka et al. [2008], and by Rodrigues et al. [2009].

The C/NOFS results from this study are different from most other studies in two important respects. First, no pre-selection of data segments was used. Second, an objective segmentation procedure was used to determine the largest data intervals that support stochastic characterization. The procedures were developed with the hope that patterns of specific structure occurrence might

reveal where enhanced intermediate-scale structure was developing within the broader ESF environment. Figure 14 shows a comparison of the most widely cited spectral characteristics and the C/NOFS results from this study. The current results suggest that developed structure extends beyond the 10 km intervals commonly sampled. On the other hand, the index distributions and, particularly, the spread in break scales suggest that a clean sampling-enhanced intermediate scale was not being achieved. This is most likely to be a consequence of elliptical C/NOFS orbit, which did not sample structure below 400 km. The wavelet-based analysis and segmentation procedures are well suited for data that present the extreme dynamic range and structure variation exemplified in Figure 2.

#### Acknowledgment

The data used for this study were made available for the study by the Air Force Research Laboratory. The MATLAB analysis procedures can be downloaded from MATLAB Central File Exchange <http://www.mathworks.com/matlabcentral/fileexchange/35092-wavelet-scale-spectra>.

#### References

- Basu, Su., S. Basu, J. P. McClure, W. B. Hanson, and H. E. Whitney (1983), High resolution topside in situ data of electron densities and VHF/GHz scintillations in the equatorial region, *J. Geophys. Res.*, *88*(A1), 403–415.
- Costa, E., E. R. de Paula, L. F. C. Rezende, K. M. Groves, P. A. Roddy, E. V. Dao, and M. C. Kelley (2011), Equatorial scintillation calculations based on coherent scatter radar and C/NOFS data, *Radio Sci.*, *46*, RS2011, doi:10.1029/2010RS004435.
- Fougere, P. F. (1985), On the accuracy of spectrum analysis of red noise processes using maximum entropy and periodogram methods' simulation studies and application to geophysical data, *J. Geophys. Res.*, *90*(A5), 4355–4366.
- Franke, S. J., and C. H. Liu (1983), Observations and modelling of multi-frequency VHF and GHz scintillations in the equatorial region, *J. Geophys. Res.*, *88*, 7075–7085.
- Hysell, D. L. (2000), An overview and synthesis of plasma irregularities in equatorial spread F, *J. Atmos. Terr. Phys.*, *62*, 1037–1056.
- Hysell, D. L., and M. C. Kelley (1997), Decaying equatorial F region plasma depletions, *J. Geophys. Res.*, *102*(A9), 20,007–20,017.
- Kelley, M. C., R. C. Livingston, C. L. Rino, and R. T. Tsunoda (1982), The vertical wave number spectrum of topside equatorial spread F: Estimates of backscatter levels and implications for a unified theory, *J. Geophys. Res.*, *87*(A7), 5217–5221.
- Livingston, R. C., C. L. Rino, J. P. McClure, and W. B. Hanson (1981), Spectral characteristics of medium-scale equatorial F region irregularities, *J. Geophys. Res.*, *86*, 2421–2428.
- Nishioka, M., Su. Basu, S. Basu, C. E. Valladares, R. E. Sheehan, P. A. Roddy, and K. M. Groves (2008), C/NOFS satellite observations of equatorial ionospheric plasma structures supported by multiple ground-based diagnostics in October 2008, *J. Geophys. Res.*, *116*, A10323, doi:10.1029/2011JA016446.
- Ouelette, N. (2012), Turbulence in two dimensions, *Phys. Today*, *65*, 68–69.
- Retterer, J. M. (2010), Forecasting low-latitude radio scintillation with 3-d ionospheric plume models: 1. Plume model, *J. Geophys. Res.*, *115*, A03306, doi:10.1029/2008JA013839.
- Rino, C. L., R. T. Tsunoda, J. Petriceks, R. C. Livingston, M. C. Kelley, and K. D. Baker (1981), Simultaneous rocket-borne beacon and in situ measurements of equatorial spread F—Intermediate wavelength results, *J. Geophys. Res.*, *86*(A4), 2411–2419.
- Rodrigues, F. S., M. C. Kelley, P. A. Roddy, D. E. Hunton, R. F. Pfaff, O. de La Beaujardiere, and G. S. Bust (2009), C/NOFS observations of intermediate and transitional scale-size equatorial spread F irregularities, *Geophys. Res. Lett.*, *36*, L00C05, doi:10.1029/2009GL038905.